Mesoscopic Fluorescence Imaging of Light-Triggered Chemotherapeutic Release in Cancer Spheroid Models

Elias Kluiszo [1], Rasel Ahmmed [1], Berna Aliu [1], Semra Aygun-Sunar[1], Matthew Willadsen[2], Hilliard L Kutscher[2], Jonathan F. Lovell[3], and Ulas Sunar[1,*]

[1] Department of Biomedical, Engineering, Stony Brook University, Stony Brook, NY 11794, USA
[2] POP Biotechnologies, Buffalo, NY 14228, USA
[3] Department of Biomedical Engineering, University at Buffalo, Buffalo, NY 14260, USA

* Correspondence; ulas.sunar@stonybrook.edu

Abstract: Peritoneal micrometastases (micromets) represent a significant clinical challenge across a wide spectrum of malignancies due to their aggressive progression and limited treatment efficacy. Liposomal Doxorubicin (Dox) is a clinically-used drug formulation that modulates the biodistribution and pharmacokinetics of the Dox chemotherapeutic, but may be hindered by slow drug release kinetics. Recent advances in this formulation enable red light-triggered release of Dox from porphyrin-phospholipid (PoP) liposome, resulting in targeted chemotherapy with reduced effects on the surrounding tissue. Light-triggered release of Dox at a tumor site functions in both a therapeutic and diagnostic capacity, as the inherent fluorescence allows for analysis of disease progression and can provide contrast for fluorescence-guided drug release and treatment. Here we examine light-triggered Dox as a contrast method for fluorescence-guided therapy by culturing the drug within a cancer spheroid model and imaging fluorescence with a laparoscopic system. Mesoscopic imaging demonstrated an increase in fluorescence signal proportional to the concentration of drug added to the cell media, and measurements correlated with plate-reader signals (Pearson R^2=0.89-0.96). Results support the use of Dox fluorescence as a contrast marker for light-triggered drug release, while PoP fluorescence provides contrast for localizing the spheroid constructs during the treatment planning.

Keywords: spatial frequency domain imaging; laparoscope; cancer spheroids; quantitative fluorescence imaging; doxorubicin drug concentration; light-triggered release; porphyrins; photodynamic therapy

1. Introduction

Peritoneal micrometastases (micromets) represent significant hurdles in the successful treatment of intra-abdominal malignancies, specifically ovarian cancer, which remains one of the most lethal gynecological diseases due to high recurrence rates [1–3]. These micromets are often too small to be detected by conventional imaging techniques such as computed tomography (CT), magnetic resonance imaging (MRI), positron emission tomography (PET), and ultrasound, which often demonstrate lower sensitivity than reassessment surgeries [4–8]. Consequently, even after surgical resection and adjuvant

chemotherapy, up to 60% of patients may still harbor occult disseminated disease [1,2,4,5,7,9]. Thus, there is an urgent need for sensitive intraoperative imaging methods that allow surgeons to visualize and selectively treat these lesions in real-time while avoiding damage to healthy tissue.

An emerging solution lies in light-activated chemo and photodynamic therapy (PDT) called chemophototherapy (CPT) [10–15]. Here, we utilize a specialized drug formulation where Doxorubicin (Dox) is encapsulated within a liposomal envelope containing porphyrin-phospholipid (PoP). While traditional systemic chemotherapy often leads to significant toxic side effects [3,7,13,15–18], these liposomal nanocarriers improve the biodistribution and efficacy of the payload ,which was suboptimal due to physical barrier [18,19]. PDT leverages light, a photosensitizing agent, and molecular oxygen to generate cytotoxic reactive oxygen species (ROS) capable of selectively destroying tumor cells [20,21]. Porphyrin-based photosensitizers preferentially accumulate in malignant cells, making PDT itself a promising surgical adjunct for treating ovarian micromet [15,22–26]. While normal tissue toxicity has hindered clinical translation, epithelial growth factor receptor (EGFR) and folate-targeted approaches [2,7,15,21,27–32] have successfully reduced peritoneal damage in animal models under semi-quantitative imaging guidance need further investigation. The lipid envelope protects the drug from degradation and facilitates passive accumulation at tumor sites via the enhanced permeability and retention (EPR) effect [6,20,33]. This PoP structure is stable in circulation but allows for controlled, site-specific delivery. By selectively permeabilizing the PoP liposomes in the presence of near-infrared light (NIR, ~660 nm) [10,11], we can improve the concentration of the drug delivered to the tumor while minimizing systemic toxicity. Porphyrin-based compounds are ideal for this dual role; they have been used in over 10 human clinical trials and naturally accumulate 2–3 fold higher in malignant cells [17,37–39].

A primary advantage of this approach is the inherent fluorescence of both the PoP carrier and the Doxorubicin payload, which enables high-sensitivity image-guided delivery. We can leverage the distinct spectral signatures of these components: PoP fluorescence is used to localize the tumor site in vivo due to its longer wavelength (~720 nm), while the fluorescent signal from Dox (~590 nm) serves as a marker to quantify drug kinetics and local release at the target [16,17]. By utilizing a laparoscope equipped with fluorescence excitation and emission filtering, these markers allow for the real-time identification of micromets during minimally invasive surgery.

However, accurately quantifying drug concentrations and penetration depths in vivo remains a challenge due to the complex optical properties of heterogeneous tissue. Approaches include wide-field [37–40], laparoscopic and endoscopic spatial frequency domain imaging (SFDI) [5], provide quantitative mapping of optical and fluorescence contrasts in tissue. To bridge the gap between monolayer cell cultures and complex animal models, 3D multicellular spheroid systems serve as a critical research tool. Unlike traditional 2D models, spheroids accurately replicate the physiological gradients, interstitial fluid pressure, and cellular architecture found in peritoneal micrometastases. These 3D systems are particularly beneficial for evaluating Dox distribution, as they allow for the study of deep-tissue drug permeation and the spatial distribution of fluorescence in a volume that mimics the occult micromets surgeons struggle to identify in the clinic.

In this work, we present a mesoscopic valuation of light-triggered drug delivery using a custom-design laparoscopic system. We utilized this system to monitor the uptake and NIR-triggered release of Dox-PoP liposomes within an ovarian cancer 3D multicellular spheroid model. By performing imaging at varied concentration, we calibrated and characterized the kinetics of Doxorubicin into the spheroids. This approach allows us to visualize the transition from the encapsulated state to the therapeutically active, diffused state of the drug. Ultimately, this study demonstrates the utility of mesoscopic

laparoscopy imaging as a powerful tool for the intraoperative assessment of nanocarrier efficacy, providing a quantitative framework for imaging and treating peritoneal micromets.

2. Results

2.1. Fluorescence Calibration in 2D Cell Culture

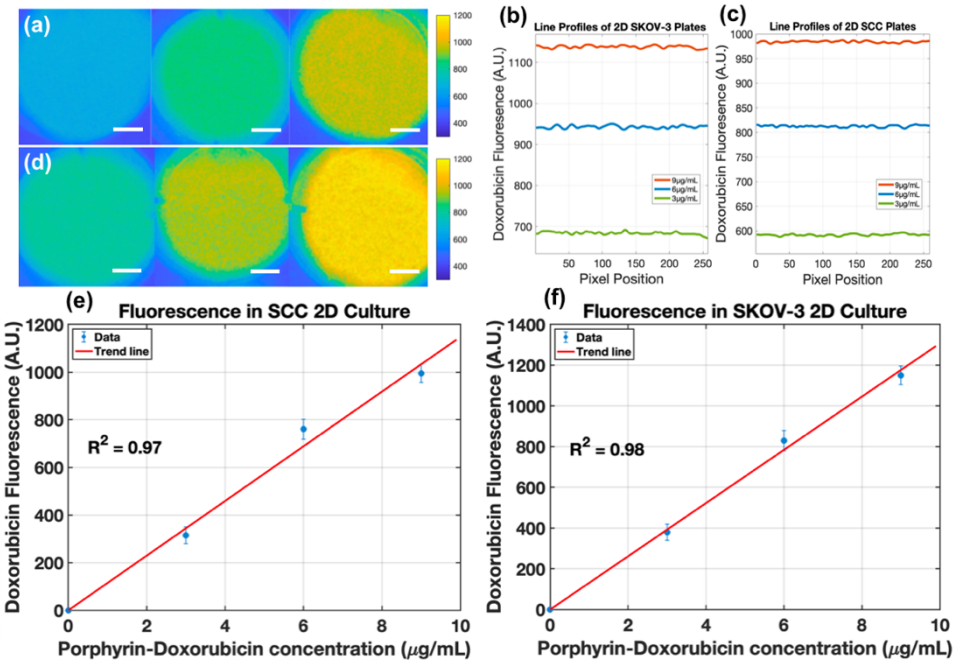

Figure 1: Fluorescent images of SCC2095sc (a) and SKOV-3 (d) cells in 2D culture, showing 3, 6, and 9 μg/mL concentrations of Doxorubicin-Porphyrin liposomes added to the cell media, after 1 min of applied activation light (scale bar = 700μm). (b) Line profile of SCC2095sc and (c) SKOV-3 images obtained at the center of the well plate (e) Linear fit of $R^2 = 0.97$ and SKOV-3 fluorescence (f) follows a $R^2 = 0.98$ linear trend.

Fluorescence imaging of the well plates with 2D culture shows accumulation of the light-activated liposomal doxorubicin within both cell lines. SKOV-3 cells exhibited a moderately higher signal intensity than the SCC2095sc cells across all corresponding drug concentrations. Both cell lines demonstrated a linear, dose-dependent response, where increasing concentrations of the liposomal formulation resulted in a proportional increase in the detected fluorescent signal after applying the activation light. Signal distribution within the wells was non-homogeneous, with a standard deviation of less than 0.15 across all wells. This indicates that the fluorescent signal is primarily localized within the individual cell bodies rather than being uniformly distributed across the growth surface.

2.2. Doxorubicin and Porphyrin Signal in Spheroid Clusters

2.2.1. Doxorubicin Signal in SCC Spheroid Clusters

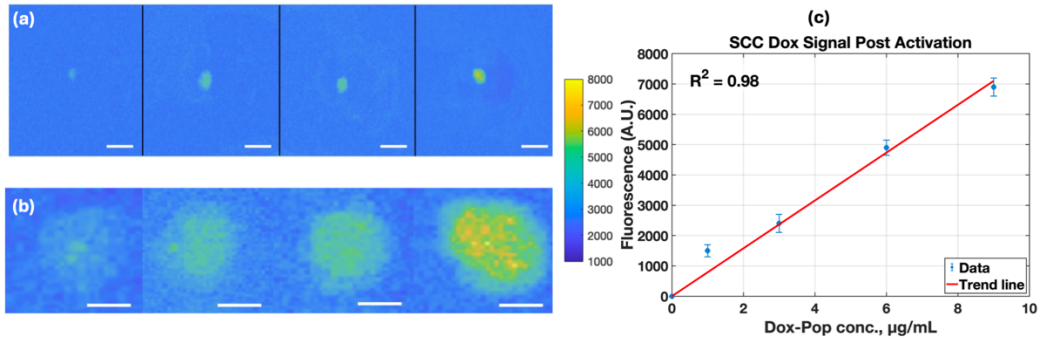

Figure 2: Mesoscopic fluorescent images of SSC cells in 24 well plates, with cultured drug concentration of 1, 3, 6, 9 µg/mL going from left to right. (a) Shows spheroid cluster with full FOV (scale bar = 700µm) and (b) displays digital zoom of fluorescent image of spheroid cluster (scale bar = 300µm). (c) Plots signal increase of spheroid cluster signal within each well with a liner trend (R^2 = 0.98) with respect to concentration.

Analysis of drug uptake in SCC2095sc spheroids demonstrated a correlation between administration levels and internal fluorescence. Across the tested concentration gradient of 1, 3, 6, and 9 µg/mL of administered Dox-PoP liposomes, a linear increase in signal was observed. Digital zoom of the cell clusters provides insight into the internal drug distribution.

2.2.2. Doxorubicin Signal in SKOV-3 Spheroid Clusters

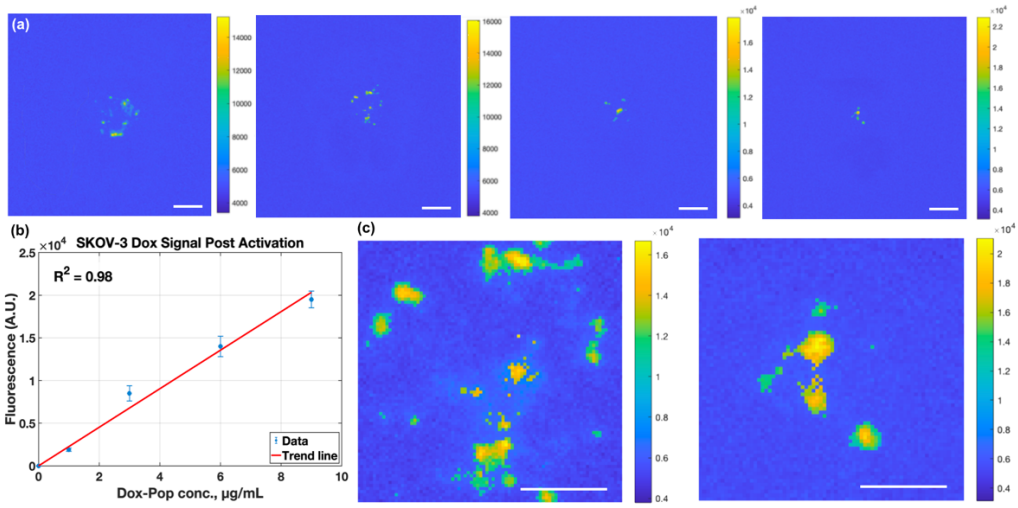

Figure **3:** Mesoscopic fluorescent images of SKOV-3 cells in 24 well plates. (a) Shows spheroid clusters with full FOV (scale bar = 700µm) with cultured drug concentration of 1, 3, 6, 9 µg/mL going from left to right. (b) Plots signal increase of upper thresholded signal within each well. (c) Displays digital zoom of fluorescent image of spheroid clusters at 3µg/mL (left) and 9µg/mL (right) (scale = 300µm).

In contrast to the compact SCC2095sc spheroids, SKOV-3 cell clusters exhibited a morphology with greater spread. Despite this structural dispersion, the spheroids maintained a dose-dependent relationship with the administered drug, showing a progressive increase in fluorescence as concentrations rose. Quantitative analysis confirmed a linear trend in the fluorescent signal across the concentration range of 1, 3, 6, and 9 μg/mL. Digital zoom of the SKOV-3 clusters further details the drug distribution, showing contrast on the spheroid cluster level. To ensure optimal visualization of the fluorescence contrast within the smaller, spread-out clusters, images were processed using independent, local colorbar scaling rather than a global intensity scale.

2.3. Validation of Fluorescence Signal

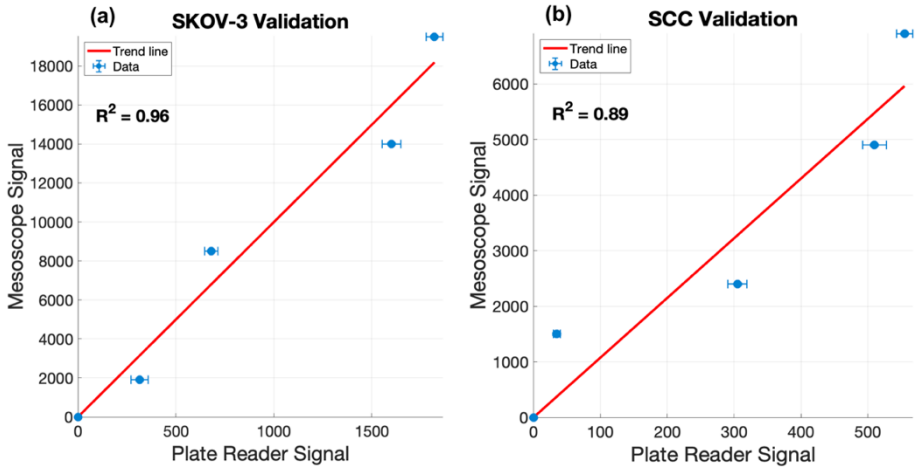

Figure 4: Released doxorubicin in spheroid clusters measured with the laparoscope vs. plate reader in SKOV-3 cells (a) and SCC2095sc cells (b) for each Dox-PoP concentration. A linear regression of these two independent methods, shown as the red line, give a Pearson's coefficient of 0.96 and 0.89 for SKOV-3 and SCC2095sc models respectively.

To validate the accuracy of the laparoscopic fluorescence signals, measurements were compared against standard well-plate reader values. Linear regression analysis was performed by plotting the mean fluorescence intensities from laparoscopic imaging against the corresponding plate reader values for each drug concentration. This allowed for the determination of Pearson's correlation coefficients as a metric of cross-platform consistency. For both cell models, a strong positive correlation was observed between the laparoscopic and plate reader measurements.

2.4. Porphyrin Signal in Spheroid Clusters

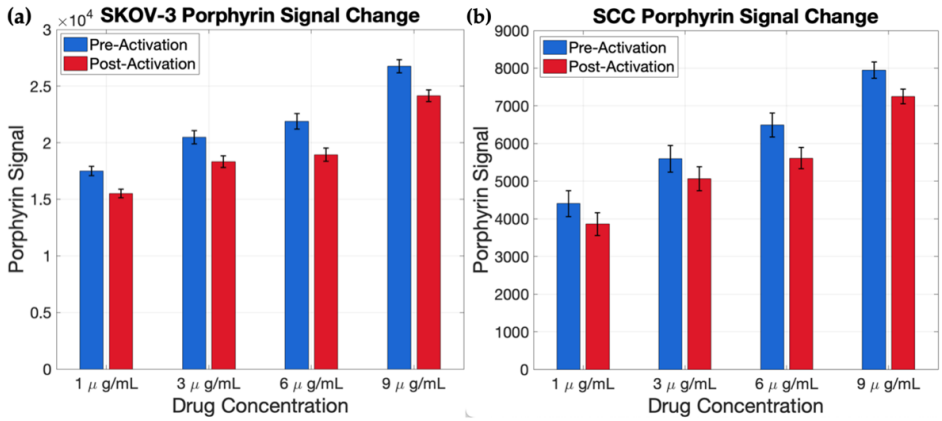

Figure 5: Averaged Porphyrin signal value from SKOV-3 (a) and SCC2095sc (b) spheroids before and after NIR light induced release, showing a slight decrease after light exposure.

Porphyrin signal from the LC-Dox-PoP liposomes was also measured before and after light-triggered release. There was a consistent decrease in porphyrin fluorescence after drug release, suggesting a degree of photobleaching occurring during the light-delivery process. Despite this slight attenuation, the porphyrin signal remained a robust indicator of the initial liposomal carrier distribution throughout the 3D spheroid architecture, with a spatial distribution that closely mirrored the doxorubicin localization within both the SCC and SKOV-3 clusters.

2.5. Microscopic Spheroid Clusters

Figure 6 presents a comparison of spheroid formation between two different cell lines, SKOV-3 and SCC2095sc 10 days after seeding. The captured micrograph highlights distinct morphological characteristics inherent to each cell model: SKOV-3 c ells exhibit less uniform aggregation, with smaller clusters and more dispersed cellular material. SCC2095sc Cells demonstrate robust spheroid development, forming densely packed, rounded structures of varying sizes. This morphological assessment is critical for validating the intact 3D structures used in subsequent fluorescence imaging experiments. By establishing these distinct cell models, the study can effectively correlate laparoscopic fluorescence signals against standard plate reader measurements to ensure cross-platform consistency.

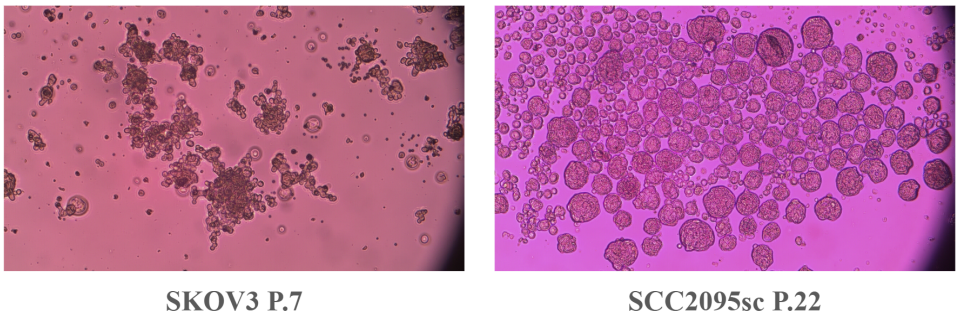

Figure 6: Comparison of spheroid formation in SCC2095sc and SKOV3 cells ten days after seeding demonstrating different morphological characteristics. Images were taken with a 10x objective lens.

3. Discussion

SCC2095sc cells consistently formed dense, uniform, and spherical aggregates characterized by strong cell-cell junctions and a smooth boundary. In contrast, SKOV-3 spheroids exhibited a dispersed morphology with greater variability in size and shape, likely due to reduced expression of adhesion molecules and a more fragmented extracellular matrix. These morphological differences [41] directly influenced the varying fluorescence signals observed between the two cell types. The compact, high-density packing of SCC2095sc spheroids created physical barriers and high interstitial pressure [42] that limited drug diffusion and reduced final signal relative to SKOV-3 spheroids. Conversely, the porous and irregular architecture of SKOV-3 clusters provided a higher effective surface area and reduced transport resistance, allowing for improved penetration of the liposomes and a higher recorded signal. Furthermore, the similarity in drug uptake profiles between SCC2095sc and SKOV-3 cells in two-dimensional culture suggests that the differences observed in the three-dimensional models are structural rather than purely biochemical.

In this model, the higher fluorescence signal observed in the spheroid center versus the periphery and 2D monolayers is likely an artifact of optical integration. Because widefield mesoscopic imaging projects 3D volumes into 2D images, the signal is integrated along the entire optical pathlength [43–45]. Thus, the thicker center of a spheroid and its stacked cellular layers yield a much higher cumulative intensity than the thinner edges or a single cell layer. Additionally, the central signal concentration likely reflects the 24-hour incubation period, which provides sufficient diffusion time for the necrotic core to act as a metabolic "sink" [46,47]. This represents a key distinction *from in vivo* tumors, where high interstitial pressure, dense matrices and limited blood flow often prevent doxorubicin from reaching the tumor center, highlighting a limitation in how spheroid models replicate complex physiological barriers.

The linear increase in signal as a function of drug concentration indicates that the uptake and delivery mechanism remains within a linear kinetic range. Across the concentration gradient of 1 to 9 μg/mL, the system does not appear to reach a saturation point for liposomal penetration [48]. This suggests that the porphyrin-loaded delivery platform provides a predictable and scalable dose-response relationship in these three-dimensional tumor models.

The experimental results demonstrated a clear correlation between the fluorescence signal and the concentration of the delivered therapeutic. In both the 2D monolayer and the 3D spheroid models [49], a proportional relationship was observed in the signals recorded from the samples. As the concentration of the drug increased, the fluorescence intensity scaled accordingly. While these initial findings suggest that the fluorescence signal may serve as a proxy for drug concentration and tumor volume, further studies involving a broader range of concentrations are required to establish a robust linear relationship and a definitive calibration curve [21]. The use of light-triggered Doxorubicin in conjunction with a filtered laparoscopic system provides a robust framework for fluorescence-guided surgery. Additionally, the spheroid model here provides a more robust estimate of in vivo drug kinetics due to the more realistic properties of the tumor microenvironment [34–36]. By successfully isolating the signals of Dox in light triggered liposomes and subtracting background artifacts via ND filtering, we have shown that it is possible to visualize simulated micromet cell clusters in an in vitro model.

4. Materials and Methods

4.1. Laparoscopic SFDI System

The laparoscopic SFDI system was constructed and validated earlier [50] as shown in Figure 7. Figure 7a shows the sample imaging setup for release experiment, and figure 7b details the projection with digital micromirror device (DMD) and imaging components within the laparoscopic system.

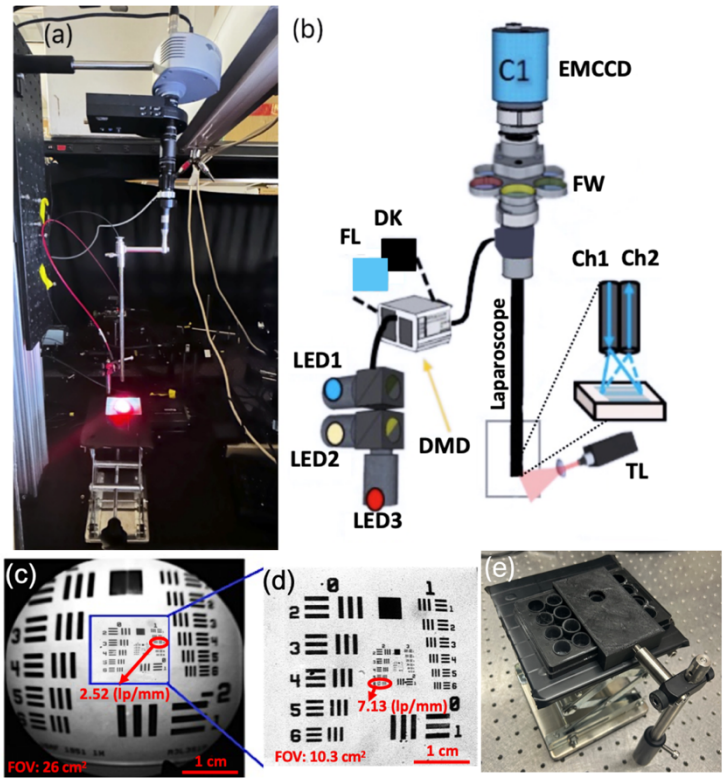

Figure 7. The experimental setup of Doxorubicin release in cell spheroid model, (a) laparoscope SFDI system picture projecting excitation light and the 660 nm treatment light in red, (b) laparoscope SFDI setup design sketch, showing component details (c) Laparoscopic image of fluorescent-positive United States Air Force (USAF) target. (d) Reflectance image of USAF target. Outlined region in (c) provides relative scale of the Fluorescence and Reflectance modalities. (e) Custom well-plate holder with a fixed viewing port and sliding track to ensure consistent spatial alignment of the well plate across sequential imaging sessions.

In our laparoscopic fluorescence imaging system, illumination was provided by three high-power LEDs at 490 nm, 590 nm, and 656 nm, which were coupled to the DMD via a liquid light guide (Mightex, Ontario, Canada). Both the LEDs and DMD were remotely controlled using MATLAB. Excitation light was projected through a 2.4 mm imaging fiber containing 13,000 elements (Asahi Kasei, Tokyo, Japan), which was coupled to a fixed laparoscope and delivered light to the distal end facing the tissue. A custom objective lens at the fiber tip collimated the output and provided uniform illumination across the tissue surface. The excitation signal were collected through the laparoscope optics, including the laparoscope (8912.43, R. Wolf, Vernon Hills, IL, USA), a zoom coupler (Accu-Beam, TTI Medical, CA, USA), two 25 mm achromatic lenses, a filter wheel, and an aperture (ThorLabs, NJ, USA), before being detected by an EMCCD camera (1004 × 1002 pixels, Luca, Andor, Belfast, Ireland). The camera was focused to capture signal over a 3.2 × 3.2 cm field of view (FOV). At a 5.1 × 5.1 cm FOV, the system could resolve group 1, element 3 of the target, corresponding to a line width of 198.43 µm, which is equivalent to 2.52 line pairs/mm as shown in Figure 7c. Figure 7d demonstrates a higher magnification (with a smaller FOV of 3.2 cm × 3.2 cm), at which the endoscopic system can resolve group 2, element 6 of the target, corresponding to line width 70.15 µm, which is equivalent to 7.13 line pairs/mm.

A 490 nm LED with a 490 ± 10 nm bandpass filter was used to excite Dox fluorescence, and the 656 nm LED was used to excite Porphyrin fluorescence. To isolate the fluorescent signal of doxorubicin, a 530 nm long-pass filter and a 593 ± 40 nm fluorescent filter were used. Neutral density (ND) filters, matched to the transmission of the fluorescent filters, are used to obtain reflectance data and remove specular reflections and signal leakages,

as described further in 4.4. To capture fluorescent signal from the porphyrin loaded liposomes, a 750 ± 50nm fluorescent filter was used with the 656nm excitation light. A custom 3D-printed black structure (Figure 7e) serves as a physical stop for multi-well plates. This ensures precise alignment and a constant imaged region across successive captures and filter changes while mitigating spectral reflections.

4.2 Preparation of long-circulating Dox in PoP Liposomes

The details of our PoP Dox liposome formulation have been described in [1,4,5]. PoP-liposomes incorporated PoP photosensitizer in a recent study for the development of improved peptide-based cancer vaccines, underscoring the versatility of the drug delivery platform [13]. Briefly, PoP-liposomes were synthesized from pyro-lipid through esterification of pyro with lyso-C16-PC, using 1-Ethyl-3-(3-dimethylaminopropyl) carbodiimide (EDC) and 4-dimethylaminopyridine (DMAP) in chloroform. The liposomes were formed by dispersing Porphyrin-lipid, PEGylated-lipid, cholesterol, and distearoylphosphatidylcholine in chloroform, followed by solvent evaporation. A 20 mg/mL lipid solution was extruded through a high-pressure lipid extruder with a 250 mM ammonium sulfate solution using polycarbonate membranes of 0.2, 0.1, and 0.08 μm pore size, sequentially stacked and passed through the extruder 10 times. Free ammonium sulfate was removed by overnight dialysis in a 10% sucrose solution with 10 mM HEPES at pH 7. Dox was loaded by incubating the liposomes at 60°C for 1 hour, achieving a loading efficacy of over 90% as confirmed by G-75 column tests. The self-assembly status and elution position of PoP-liposomes were tracked using 420 nm excitation and 670 nm emission, while Dox was detected using 480 nm excitation and 590 nm emission in a fluorescence plate reader (TECAN Safire).

4.3 Spheroid Model

Human epithelial ovarian adenocarcinoma cell lines SKOV-3 were purchased from the American Type Culture Collection (ATCC, HTB-77, Manassas, VA, USA) and were maintained in McCoy's 5A medium supplemented with 10% Fetal Bovine Serum (FBS) and 1% antibiotic-antimycotic. Human oral squamous cell carcinoma (OSCC) SCC2095sc (gift from Professor S. Mallery, Ohio State University) were cultured in Advanced DMEM-Serum Reduced Medium supplemented with 1% L-Glutamine, 5% heat-inactivated FBS, and 1% antibiotic- antimycotic. Media and supplements were purchased from Gibco (Grand Island, NY, USA). Cells were cultured at 37°C with 5% CO_2 in a humidified incubator. Upon reaching 80–90% confluence, cells were harvested using 0.25% trypsin-EDTA and passaged at a 1:3 ratio. To facilitate three-dimensional (3D) spheroid formation, 12-well plates were coated with Poly (2-hydroxyethyl methacrylate) (Poly-HEMA; Sigma-Aldrich) to create non-adherent surfaces. A 1.2% (w/v) Poly-HEMA working solution in 95% ethanol was applied to each well (240 μL/well) and allowed to dry for 24–48 hours at room temperature. Prior to seeding, plates were sterilized via UV exposure for 30 minutes and rinsed twice with PBS and once with Hank's balanced salt solution (HBSS). Spheroids were generated by seeding 10,000 viable cells per well into the Poly-HEMA-coated plates. The final volume in each well was adjusted to 1 mL with complete growth media. Spheroid morphology, growth, and integrity were monitored longitudinally (from Day 0 to Day 15) using an inverted microscope. Qualitative assessments focused on spheroid shape, compactness, and the presence of cellular debris.

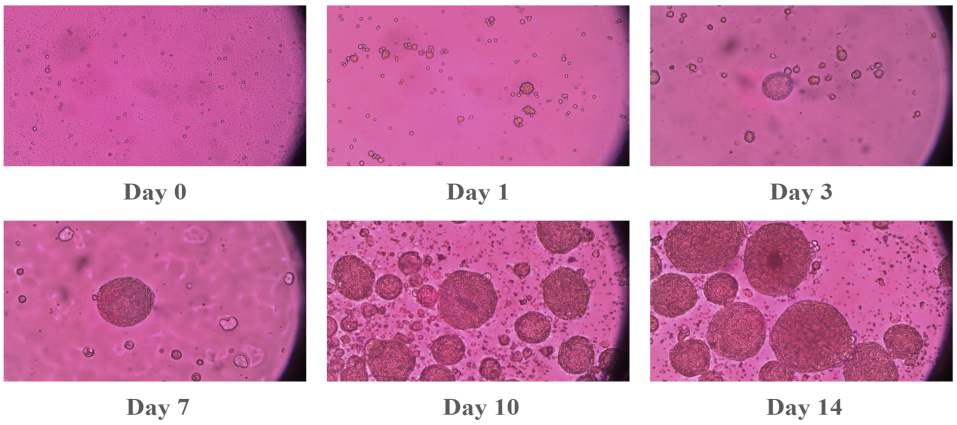

Figure 8: Spheroid formation of SCC2095sc cells. Spheroid formation was monitored at different 8 points (1, 3, 7, 10, and 14 days after seeding the cells). Images were obtained via an inverted microscope using a 20x objective.

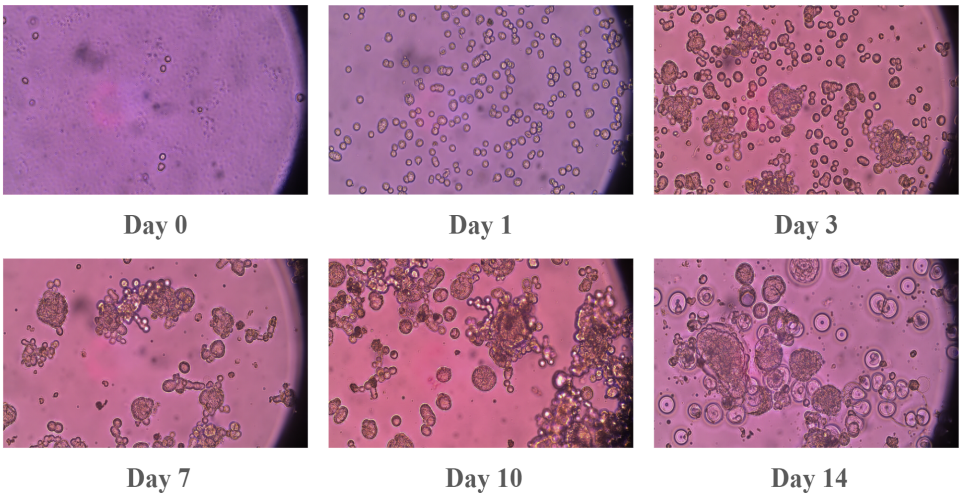

Figure 9: Spheroid formation of SKOV-3 cells. Spheroid formation was monitored at different time points (1, 3, 7, 10, and 14 days after seeding the cells). Images were obtained via an inverted microscope using a 20x objective.

Chemophototherapy was performed using a porphyrin-phospholipid liposomal formulation of doxorubicin (LC-Dox-PoP) described in 4.4. Experiments were initiated once spheroids reached maturity, typically 14–16 days post-seeding for SKOV-3 and 10–12 days for SCC2095sc. Spheroids were treated with LC-Dox-PoP at final concentrations of 1, 3, 6, and 9 μg/mL. Control groups received complete growth medium without the drug and "blank" well plates with drug concentrations but no cell presence were used for fluorescence signal calculation (see 4.4). To ensure uniform drug distribution, a designated volume of medium was replaced or supplemented with the LC-Dox-PoP working solution to reach the target concentrations. Following drug administration, plates were protected from light and incubated for 24 hours. Fluorescence imaging was performed prior to and immediately after light triggered release of LC-Dox-PoP liposomes via exposure to a 650 nm laser of 350 mW/cm^2 fluence for 1 minute per well. After mesoscopic imaging, well plates were rinsed three times with PBS and filled with phenol-red free media prior to well plate imaging at Ex = 480 nm, Em = 590 nm (TECAN Infinite M Plex).

4.4 Fluorescent Imaging and Image Processing

Prior to imaging the spheroid clusters, calibration images of dark signal, drug filled wells without cells and water filled wells are taken at all filters to account for sensor noise,

extracellular drug fluorescence and leakages respectively. For each experimental well, the doxorubicin and porphyrin signals were captured by illuminating the samples at their respective excitation peaks using the appropriate fluorescent and ND filters. Following this initial characterization, activation light was applied to trigger drug release, after which the fluorescent signals were re-imaged to quantify the change in localized drug concentration.

To correct for excitation light leakage into the fluorescence detection channel, an excitation-only reference image was acquired immediately prior to each fluorescence image under identical excitation conditions using a neutral-density (ND) filter with the same optical density (OD) value as the respective porphyrin and doxorubicin fluorescent filters. After dark subtraction, the ND image is assumed to be a linearly scaled version of leakages in the image taken with the fluorescent filters with the same OD blocking filters. To derive this scaling factor, calibration images without fluorophores (water filled wells of identical volume to cell wells) were taken prior to fluorescence imaging at all filter configurations, where the true fluorescence signal is 0. We then perform an Ordinary Least Squares regression over these images to determine our scaling factor α:

$$\alpha = \frac{\sum_{(x,y)} F(x,y) \cdot ND(x,y)}{\sum_{(x,y)} (ND(x,y))^2} \tag{1}$$

Where (x,y) is the set of pixel coordinates for the ND and fluorescent (F) images. To prevent overcorrection, a spatially weighted mask (M) is derived from the normalized signal from the ND filter. Then, the weighted and scaled leakage estimate is subtracted from the processed fluorescence image:

$$F_{corr}(x,y) = F(x,y) - [\alpha \cdot ND(x,y) \cdot M(x,y)] \tag{2}$$

This method corrects for leakage at the cell level, which would be standard across the well plate, and leakage due to reflections caused by the plastic well plate material that could confound signal. This approach preserves linearity, accounts for spatially localized leakage, and minimizes subtraction of true fluorescence signal.

Final quantification of the drug signal was achieved through segmentation, defined by the selection of pixels with intensity values exceeding a threshold that corresponded to the background fluorescence of the culture media. This segmentation process ensured that the average signal intensity reflected only the drug accumulated within the cellular structures, providing a representation of the uptake and release kinetics within the spheroid clusters specifically.

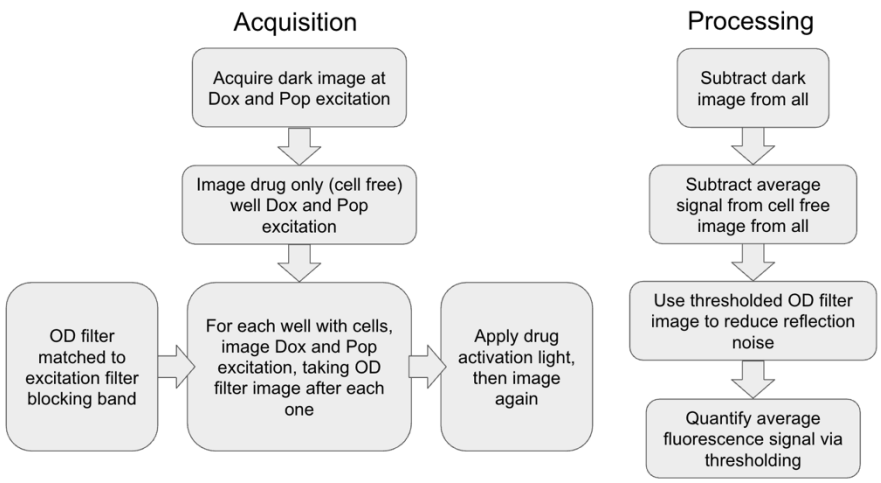

Figure 10: Flowchart of fluorescent imaging and post-processing.

5. Conclusions

This study demonstrates a laparoscopic fluorescence imaging system capable of accurately monitoring therapeutic uptake in 3D spheroid models. Fluorescence signal was positively correlated with cell count and drug concentration, indicating a proportional uptake of the therapeutic by the spheroids and 2D cells. To ensure the accuracy of these signals, we validated the laparoscopic measurements against standard well-plate readers, observing a strong positive correlation and high cross-platform consistency across all tested cell lines. The performance of the system was supported by several key technical implementations such as signal isolation (i.e. proper fluorescence filters), artifacts minimization (i.e. OD filter) and spatial standardization (i.e. 3D printed structure). These findings highlight the potential of these fluorescent markers as contrast agents for fluorescence-guided tumor localization and drug release for optimal elimination of micromets. Future work will focus on *in vivo* validation to assess the system's performance against the complex optical background of the live peritoneum.

Acknowledgments: The authors acknowledge the funding support from NIH/NCI R01 (5R01CA243164-06). We also thank Professor Susan R. Mallery (The Ohio State University) for providing SCC20905sc cells.

Author Contributions: U.S. conceived and designed the experiments; R.A. designed the device, E.K, SAS, B.A. performed the experiments; E.K. analyzed the data; R.A., U.S., E.K., SAS wrote the paper.

Funding: This research was funded by NIH/NCI R01 (5R01CA243164-06).

Institutional Review Board Statement: "Not applicable."

Informed Consent Statement: "Not applicable."

Data Availability Statement: The data that support the findings of this study are available from the corresponding author upon reasonable request.

Conflicts of Interest: The authors declare no conflict of interest. The funding sponsors had no role in the design of the study, in the collection, analysis, or interpretation of data, in the writing of the manuscript, and in the decision to publish the results.

References

1. A. B. Alvero, D. Kim, E. Lima, N. J. Sumi, J. S. Lee, C. Cardenas, M. Pitruzzello, D.-A. Silasi, N. Buza, T. Fahmy, and G. Mor, "Novel approach for the detection of intraperitoneal micrometastasis using an ovarian cancer mouse model," Sci. Rep. **7**(1), 40989 (2017).
2. H. Azaïs, C. Schmitt, M. Tardivel, O. Kerdraon, A. Stallivieri, C. Frochot, N. Betrouni, P. Collinet, and S. Mordon, "Assessment of the specificity of a new folate-targeted photosensitizer for peritoneal metastasis of epithelial ovarian cancer to enable intraperitoneal photodynamic therapy. A preclinical study," Photodiagnosis Photodyn. Ther. **13**, 130–138 (2016).
3. J. K. Chan, B. J. Monk, D. Cuccia, H. Pham, S. Kimel, M. Gu, M. J. Hammer-Wilson, L.-H. L. Liaw, K. Osann, P. J. DiSaia, M. Berns, B. Tromberg, and Y. Tadir, "Laparoscopic Photodynamic Diagnosis of Ovarian Cancer Using 5-Aminolevulinic Acid in a Rat Model," Gynecol. Oncol. **87**(1), 64–70 (2002).
4. K. B. Mathieu, D. G. Bedi, S. L. Thrower, A. Qayyum, and R. C. Bast Jr, "Screening for ovarian cancer: imaging challenges and opportunities for improvement," Ultrasound in Obstetrics & Gynecology **51**(3), 293–303 (2018).
5. J. Kress, D. J. Rohrbach, K. A. Carter, D. Luo, C. Poon, S. Aygun-Sunar, S. Shao, S. Lele, J. F. Lovell, and U. Sunar, "A dual-channel endoscope for quantitative imaging, monitoring, and triggering of doxorubicin release from liposomes in living mice," Sci. Rep. **7**(1), 15578 (2017).
6. M. S. Gatto, M. P. Johnson, and W. Najahi-Missaoui, "Targeted Liposomal Drug Delivery: Overview of the Current Applications and Challenges," . **14**(6), (2024).
7. T. Sugiyama, T. Nishida, K. Komai, H. Nishimura, M. Yakushiji, and H. Nishimura, "Comparison of CA 125 assays with abdominopelvic computed tomography and transvaginal ultrasound in monitoring of ovarian cancer," International Journal of Gynecology & Obstetrics **54**(3), 251–256 (1996).
8. P. G. Rose, P. Faulhaber, F. Miraldi, and F. W. Abdul-Karim, "Positive emission tomography for evaluating a complete clinical response in patients with ovarian or peritoneal carcinoma: Correlation with second-look laparotomy," Gynecol. Oncol. **82**(1), 17–21 (2001).
9. M. Longmire, N. Kosaka, M. Ogawa, P. L. Choyke, and H. Kobayashi, "Multicolor in vivo targeted imaging to guide real-time surgery of HER2-positive micrometastases in a two-tumor coincident model of ovarian cancer," Cancer Sci. **100**(6), 1099–1104 (2009).
10. D. Luo, K. A. Carter, A. Razi, J. Geng, S. Shao, D. Giraldo, U. Sunar, J. Ortega, and J. F. Lovell, "Doxorubicin encapsulated in stealth liposomes conferred with light-triggered drug release," Biomaterials **75**, 193–202 (2016).
11. K. A. Carter, S. Shao, M. I. Hoopes, D. Luo, B. Ahsan, V. M. Grigoryants, W. Song, H. Huang, G. Zhang, R. K. Pandey, J. Geng, B. A. Pfeifer, C. P. Scholes, J. Ortega, M. Karttunen, and J. F. Lovell, "Porphyrin–phospholipid liposomes permeabilized by near-infrared light," Nat. Commun. **5**(1), 3546 (2014).
12. J. Kress, D. J. Rohrbach, K. A. Carter, D. Luo, S. Shao, S. Lele, J. F. Lovell, and U. Sunar, "Quantitative imaging of light-triggered doxorubicin release," Biomed. Opt. Express **6**(9), 3546–3555 (2015).
13. D. Miranda and J. F. Lovell, "Mechanisms of light-induced liposome permeabilization," Bioeng. Transl. Med. **1**(3), 267–276 (2016).
14. D. J. Rohrbach, K. A. Carter, D. Luo, S. Shao, S. Aygun-Sunar, J. F. Lovell, and U. Sunar, "Fluence Rate-Dependent Kinetics of Light-Triggered Liposomal Doxorubicin Assessed by Quantitative Fluorescence-Based Endoscopic Probe," Int. J. Mol. Sci. **26**(3), (2025).
15. D. Luo, K. A. Carter, D. Miranda, and J. F. Lovell, "Chemophototherapy: An Emerging Treatment Option for Solid Tumors," Advanced Science **4**(1), 1600106 (2017).
16. M. Kauffman, M. E. Kauffman, H. Zhu, Z. Jia, and Y. Li, "Fluorescence-Based Assays for Measuring Doxorubicin in Biological Systems.," Reactive oxygen species **2 6**, 432–439 (2016).
17. H. Sparks, H. Kondo, S. Hooper, I. Munro, G. Kennedy, C. Dunsby, P. French, and E. Sahai, "Heterogeneity in tumor chromatin-doxorubicin binding revealed by in vivo fluorescence lifetime imaging confocal endomicroscopy," Nat. Commun. **9**(1), 2662 (2018).
18. B. Q. Spring, A. O. Abu-Yousif, A. Palanisami, I. Rizvi, X. Zheng, Z. Mai, S. Anbil, R. B. Sears, L. B. Mensah, R. Goldschmidt, S. S. Erdem, E. Oliva, and T. Hasan, "Selective treatment and monitoring of disseminated cancer micrometastases in vivo using dual-function, activatable immunoconjugates," Proceedings of the National Academy of Sciences **111**(10), E933–E942 (2014).

19. S.-D. Li and L. Huang, "Pharmacokinetics and Biodistribution of Nanoparticles," Mol. Pharm. **5**(4), 496–504 (2008).
20. M. D. Fulton and W. Najahi-Missaoui, "Liposomes in Cancer Therapy: How Did We Start and Where Are We Now," Int. J. Mol. Sci. **24**(7), (2023).
21. W. Zhong, J. P. Celli, I. Rizvi, Z. Mai, B. Q. Spring, S. H. Yun, and T. Hasan, "In vivo high-resolution fluorescence microendoscopy for ovarian cancer detection and treatment monitoring," Br. J. Cancer **101**(12), 2015–2022 (2009).
22. N. Staropoli, D. Ciliberto, C. Botta, L. Fiorillo, A. Grimaldi, S. Lama, M. Caraglia, A. Salvino, P. Tassone, and P. Tagliaferri, "Pegylated liposomal doxorubicin in the management of ovarian cancer," Cancer Biol. Ther. **15**(6), 707–720 (2014).
23. S. Boussios and K. H. Katsanos, *Systemic Treatment-Induced Gastrointestinal Toxicity: Incidence, Clinical Presentation and Management SEE PROFILE* (2012).
24. U. Sunar, D. J. Rohrbach, J. Morgan, N. Zeitouni, and B. W. Henderson, "Quantification of PpIX concentration in basal cell carcinoma and squamous cell carcinoma models using spatial frequency domain imaging," Biomed. Opt. Express **4**(4), 531–537 (2013).
25. W. Mo, D. J. Rohrbach, and U. Sunar, "Imaging a photodynamic therapy photosensitizer in vivo with a time-gated fluorescence tomography system," J. Biomed. Opt. **17**(7), 71306 (2012).
26. S. Mallidi, S. Anbil, A.-L. Bulin, G. Obaid, M. Ichikawa, and T. Hasan, "Beyond the Barriers of Light Penetration: Strategies, Perspectives and Possibilities for Photodynamic Therapy," Theranostics **6**, 2458–2487 (2016).
27. S. Wang, G. Hüttmann, T. Scholzen, Z. Zhang, A. Vogel, T. Hasan, and R. Rahmanzadeh, "A light-controlled switch after dual targeting of proliferating tumor cells via the membrane receptor EGFR and the nuclear protein Ki-67," Sci. Rep. **6**(1), 27032 (2016).
28. B. Q. Spring, R. Bryan Sears, L. Z. Zheng, Z. Mai, R. Watanabe, M. E. Sherwood, D. A. Schoenfeld, B. W. Pogue, S. P. Pereira, E. Villa, and T. Hasan, "A photoactivable multi-inhibitor nanoliposome for tumour control and simultaneous inhibition of treatment escape pathways," Nat. Nanotechnol. **11**(4), 378–387 (2016).
29. J. P. Celli, I. Rizvi, A. R. Blanden, I. Massodi, M. D. Glidden, B. W. Pogue, and T. Hasan, "An imaging-based platform for high-content, quantitative evaluation of therapeutic response in 3D tumour models," Sci. Rep. **4**(1), 3751 (2014).
30. C. Sheng, P. Jack Hoopes, T. Hasan, and B. W. Pogue, "Photobleaching-based Dosimetry Predicts Deposited Dose in ALA-PpIX PDT of Rodent Esophagus," Photochem. Photobiol. **83**(3), 738–748 (2007).
31. C. Sheng, B. W. Pogue, E. Wang, J. E. Hutchins, and P. J. Hoopes, "Assessment of Photosensitizer Dosimetry and Tissue Damage Assay for Photodynamic Therapy in Advanced-stage Tumors," Photochem. Photobiol. **79**(6), 520 – 525 (2004).
32. Q. G. A. H. B. C. K. O. T. M. J. G. F. C. B. N. C. P. M. S., "Fischer 344 Rat: A Preclinical Model for Epithelial Ovarian Cancer Folate-Targeted Therapy," Int J Gynecol Cancer **25**(7), 1194–1200 (2015).
33. M. Vinci, S. Gowan, F. Boxall, L. Patterson, M. Zimmermann, W. Court, C. Lomas, M. Mendiola, D. Hardisson, and S. A. Eccles, "Advances in establishment and analysis of three-dimensional tumor spheroid-based functional assays for target validation and drug evaluation," BMC Biol. **10**(1), 29 (2012).
34. M. C. Decarli, R. Amaral, D. P. dos Santos, L. B. Tofani, E. Katayama, R. A. Rezende, J. V. L. da Silva, K. Swiech, C. A. T. Suazo, C. Mota, L. Moroni, and Â. M. Moraes, "Cell spheroids as a versatile research platform: formation mechanisms, high throughput production, characterization and applications," Biofabrication **13**(3), 32002 (2021).
35. I. Mó, I. J. Sabino, D. de Melo-Diogo, R. Lima-Sousa, C. G. Alves, and I. J. Correia, "The Importance of Spheroids in Analyzing Nanomedicine Efficacy," Nanomedicine **15**(15), 1513–1525 (2020).
36. G. Mehta, A. Y. Hsiao, M. Ingram, G. D. Luker, and S. Takayama, "Opportunities and challenges for use of tumor spheroids as models to test drug delivery and efficacy," Journal of Controlled Release **164**(2), 192–204 (2012).
37. S. Ségaud, L. Baratelli, E. Felli, E. Bannone, L. Cinelli, M. R. Rodríguez-Luna, N. Okamoto, D. S. Keller, M. de Mathelin, S. Lecler, M. Diana, and S. Gioux, "Trident: A dual oxygenation and fluorescence imaging platform for real-time and quantitative surgical guidance," Frontiers in Photonics **Volume 3-2022**, (2022).
38. R. Meijer, L. van Manen, H. H. Hartgrink, J. Burggraaf, S. Gioux, A. L. Vahrmeijer, and J. S. D. Mieog, "Quantitative dynamic near-infrared fluorescence imaging using indocyanine green for analysis of bowel perfusion after mesenteric resection," J. Biomed. Opt. **26**(6), 60501 (2021).
39. S. Gioux, A. Stockdale, R. Oketokoun, Y. Ashitate, N. J. Durr, L. A. Moffitt, J. V. F. M.D., A. Mazhar, B. J. Tromberg, A. J. Durkin, B. T. Lee, S. J. Lin, A. M. Tobias, D. J. Cuccia, E. Kelly, and M. Weinmann, "First-in-

human pilot study of a spatial frequency domain oxygenation imaging system," J. Biomed. Opt. **16**(8), 86015 (2011).

40. J. P. Angelo, M. van de Giessen, and S. Gioux, "Real-time endoscopic optical properties imaging," Biomed. Opt. Express **8**(11), 5113–5126 (2017).
41. K. L. Sodek, M. J. Ringuette, and T. J. Brown, "Compact spheroid formation by ovarian cancer cells is associated with contractile behavior and an invasive phenotype," Int. J. Cancer **124**(9), 2060–2070 (2009).
42. M. A. Swartz and A. W. Lund, "Lymphatic and interstitial flow in the tumour microenvironment: linking mechanobiology with immunity," Nat. Rev. Cancer **12**(3), 210–219 (2012).
43. Y. Imamura, T. Mukohara, Y. Shimono, Y. Funakoshi, N. Chayahara, M. Toyoda, N. Kiyota, S. Takao, S. Kono, T. Nakatsura, and H. Minami, "Comparison of 2D- and 3D-culture models as drug-testing platforms in breast cancer," Oncol. Rep. **33**(4), 1837–1843 (2015).
44. A. Alfonso-Garcia, J. Bec, B. Weyers, M. Marsden, X. Zhou, C. Li, and L. Marcu, "Mesoscopic fluorescence lifetime imaging: Fundamental principles, clinical applications and future directions," J. Biophotonics **14**(6), e202000472 (2021).
45. A. I. Minchinton and I. F. Tannock, "Drug penetration in solid tumours," Nat. Rev. Cancer **6**(8), 583–592 (2006).
46. J. K. Lukowski, E. M. Weaver, and A. B. Hummon, "Analyzing Liposomal Drug Delivery Systems in Three-Dimensional Cell Culture Models Using MALDI Imaging Mass Spectrometry," Anal. Chem. **89**(16), 8453–8458 (2017).
47. F. Yang, S. S. Teves, C. J. Kemp, and S. Henikoff, "Doxorubicin, DNA torsion, and chromatin dynamics," Biochimica et Biophysica Acta (BBA) - Reviews on Cancer **1845**(1), 84–89 (2014).
48. A. Tivnan, W. S. Orr, V. Gubala, R. Nooney, D. E. Williams, C. McDonagh, S. Prenter, H. Harvey, R. Domingo-Fernández, I. M. Bray, O. Piskareva, C. Y. Ng, H. N. Lode, A. M. Davidoff, and R. L. Stallings, "Inhibition of Neuroblastoma Tumor Growth by Targeted Delivery of MicroRNA-34a Using Anti-Disialoganglioside GD2 Coated Nanoparticles," PLoS One **7**(5), e38129- (2012).
49. J. Friedrich, C. Seidel, R. Ebner, and L. A. Kunz-Schughart, "Spheroid-based drug screen: considerations and practical approach," Nat. Protoc. **4**(3), 309–324 (2009).
50. R. Ahmmed, E. Kluiszo, S. Aygun-Sunar, M. Willadsen, H. L. Kutscher, J. F. Lovell, and U. Sunar, "Quantitative Fluorescence Imaging of Chemophototherapy Drug Pharmacokinetics Using Laparoscopic SFDI," Int. J. Mol. Sci. **26**(12), (2025).